Bubbles in a Fluidized Bed: A Fast X-Ray Scanner

R. F. Mudde
Kramers Laboratorium voor Fysische Technologie,
Delft University of Technology, 2628 BW Delft, The Netherlands

DOI 10.1002/aic.12469
Published online November 29, 2010 in Wiley Online Library (wileyonlinelibrary.com).

We present experiments on a bubble train in a 23-cm-diameter fluidized bed of a Geldart B powder. The bubbles are injected via a single capillary inserted in the bed. We use our double X-ray tomographic scanner to measure the solids distribution in two parallel cross sections of the bed. We report data for four different heights of the measuring planes above the capillary outlet. The velocity of individual bubbles is found from the time of flight from the lower to the upper plane. We have done separate calibration experiments for the velocity. In this article, we present data for the size and velocity of individual bubbles. From the bubble velocity, we could obtain the vertical dimension of the bubbles. This makes it possible to measure the volume of each bubble. The results show that our scanner is capable of measuring properties of bubbles with a size of 2.5 cm and above. © 2010 American Institute of Chemical Engineers *AIChE J,* 57: 2684–2690, 2011

Keywords: X-ray tomography, time resolved, spatial resolution, SART, bubbling fluidized bed

Introduction

Gas–solid fluidization is one of the various operations used in chemical engineering in which granular material is manipulated by a gas flow. It has as specific feature that it deals with dense multiphase flows, i.e., the local volume fraction of particles is high, on the order of 30–60%. These systems can be described at different levels of detail, from course models at the reactor level to detailed ones that use a three-dimensional continuum description to approaches that track individual particles. Especially, these sophisticated approaches require detailed experimental data for comparison and guidance. However, experimentalists are confronted with great challenges when trying to obtain the hydrodynamical information at the required level of detail and accuracy. This is by and large due to the opaqueness of the fluidized systems: laser-based techniques are of very limited use. Alternative techniques, Such as electrical capacitance tomography (ECT), magnetic resonance imaging (MRI), and nuclear densitometry have been developed. With these techniques, tomographic reconstructions of the density distribution inside the fluidized bed can be made. ECT is popular: it is relatively cheap and fast, giving a high temporal resolution. Tomographic reconstructions of a plane can be made at rates of several hundreds per second.[1–3] In contrast to the speed, the spatial resolution of ECT is a difficult topic. Warsito and Fan have used neural networks and a multicriterion optimization to increase the spatial resolution.[4] They also used a double ring of sensors. This gave them the possibility to measure across the two planes defined by the two sets of sensors, thereby extending their technique to 3D reconstruction.[5] However, ECT relies on so-called soft fields. Consequently, a change in the electromagnetic properties in one location changes the field everywhere in the domain. This makes reconstruction difficult, and the resolution in the center of the object is usually relatively poor. A more recent development in experiments on multiphase flows and reactors is MRI.[6] MRI is based on the magnetic moment of a nuclear particle like a proton. The system is placed in a strong, uniform magnetic field that will align the nuclear spins. By

Correspondence concerning this article should be addressed to R. F. Mudde at r.f.mudde@tudelft.nl.

© 2010 American Institute of Chemical Engineers

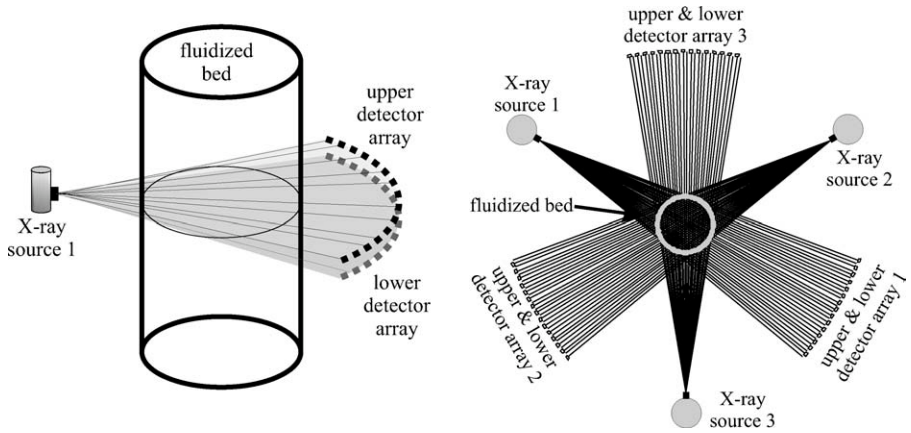

Figure 1. Schematic of the X-ray scanner. Left: side view showing for clarity only one source with its two detector arrays, right: top view.

pulsing with a small, secondary magnetic field these spins can be kicked out of their alignment. The spins will relax back to their equilibrium distribution. By following this relaxation process, the amount of spins, which is directly related to the amount of, e.g., hydrogen atoms, can be traced. Evidently, this can be translated to species concentration. MRI has a very high spatial resolution, it is not as fast as ECT, but it can not only find the solids distribution (in three dimensions!) but also find the velocity. However, the magnetic field needs to be very strong making applications at decimeter scale, as is required for fluidization, difficult, and expensive.

Solids are to some extent transparent to X-ray or γ-radiation. Therefore, nuclear techniques are also candidates for experiments on fluidized systems. In Ref. 7, the use of nuclear techniques in opaque multiphase systems is reviewed. The radiation can be used to measure the volume fraction of gas (or equivalent of the solids) in a fluidized bed. However, it is also possible to make one (or more) of the particles radioactive and use it as a flow follower. At least two different variations are in use: CARPT (computer automated radioactive particle tracking) developed by Dudukovic and coworkers[8–12] and PEPT (positron emission particle tracking) as is used, e.g., in Refs. 13 and 14.

The volume fraction distribution in a cross section of the fluidized bed can be found using the attenuation of the radiation. This is referred to as "nuclear densitometry". This is not only applicable to fluidized beds, see, e.g., Refs. 15 and 16. For instance, Ref. 17 obtained the volume fraction in a gas–liquid bubble column with a diameter of 48 cm. They used a single beam-detector pair to perform scans over a horizontal cross section of the column assuming cylinder symmetry. Ref. 18 followed a similar procedure to measure the solids volume fraction in a turbulent fluidized bed of 40 cm. Fan beams that scan a plane simultaneously are also in use, see, e.g., Ref. 16 which used a fan beam from a single γ source with multiple detectors. They rotated the source-detector combination around their bubble column obtaining a large number of projections. This increases the spatial resolution significantly. The total measuring time is about 1 h and only a time-averaged volume fraction can obtained. This type of tomographic reconstruction is referred to as computed tomography or CT. In medical imaging, the use of X-ray tomography is standard practice. The source-detector system again rotates around the patient. This way high resolution, static images can be produced. Obviously, for flowing systems like fluidized beds, this is not an option if local information both in time and space is required.

X-ray tomographic systems can be made fast by using, e.g., multiple X-ray sources simultaneously. Hampel and coworkers developed a different approach.[19,20] In their setup, X-rays are generated by moving an electron beam at high speed over a Tungsten bar. This way, tomographic images up to a rate of 10,000 frames per second can be made.

In this article, we report experiments using a three-source X-rays scanner and a 23-cm fluidized bed. The scanner measures simultaneously in two parallel planes, separated by a small, vertical distance. We describe experiments using a hollow cylinder that is pulled upward through the fluidized bed. This allows us to accurately calibrate velocity measurements of bubbles in a fluidized bed. We further report measurements of a train of bubbles generated from a single capillary inserted in the fluidized bed. These bubbles rise upward through the bed in a train. We measure at different heights above the bubble injector and study the evolution of the bubble train.

Experimental Setup

A 23-cm inner-diameter perspex tube (wall thickness 5 mm) forms the fluidized bed. It is filled with 0.56-mm sized polystyrene particles (solids density 1102 kg/m^3). This is a Geldart B powder. The minimum fluidization velocity is 0.12 m/s. The air (room temperature) is via a wind box supplied to the bed through a porous plate (sintered bronze, pore size 30–70 μm, plate thickness 7 mm). The ungassed bed height is 59 cm. A schematic of a fluidized bed with two bubbles in the measuring plane of the densitometer is given in Figure 1.

The X-ray sources are placed at 120° around the fluidized bed. Each source generates a fan beam that is detected by two sets of 32 sensors placed opposite of the source. By using two sets, two measuring planes are formed. The distance between the planes is about 1.9 cm. The true distance needs to follow from a calibration experiment, which will be discussed later. The distance from the X-ray target to the

center of the fluidized bed is 71.5 cm and from X-ray target to the detectors is 157 cm. The fluidized bed is placed on a table that can be moved up and down in the vertical direction. This way we can adjust the height of the measuring plane in the column.

The X-ray sources used are manufactured by Yxlon International GmbH. The maximum X-ray energy is 150 keV. We operate the sources at a low energy flux with a tube current usually less than 1 mA. The detectors all consist of a $CdWO_4$ scintillation crystal optically coupled to a PIN photodiode. They are manufactured by Hamamatsu (type: S 1337 - 1010BR). Their crystal size is 10 mm $\times$ 10 mm $\times$ 10 mm.

A plastic casing in the form of an arc holds two horizontal arrays of 32 detectors. The curvature of the array is such that the distance to the focal point of the source is equal for all detectors. Of these detectors, 30 are used to produce data for tomographic reconstruction, and the two outermost detectors are used to monitor the alignment of the object vessel and proper functioning of the tomographic system. The data are collected simultaneously at a sampling frequency of 2500 Hz, both for the upper and lower ring of detectors. The measured data are read out using a 12-bit ADC card and stored on the computer. The entire process is controlled via a workstation that sends out the trigger signals to the sources and reads out the detectors. The data are processed off line.

Tomographic Reconstruction

Measuring principle

We use the algebraic reconstruction technique (ART) for reconstructing the solids distribution in the measuring planes. The measuring principle is based on the attenuation of the X-rays that pass through a certain material. For monochromatic radiation through a homogeneous slab of material, the attenuation of the incoming radiation is described by the Lambert–Beer law:

$$I = I_0 e^{-\mu x}, \tag{1}$$

where I_0 is the photon intensity registered per second when the system is in vacuum, μ denotes the linear absorption coefficient of the material of the slab, and x is the slab thickness. When radiating with a single, thin beam of photons through a fluidized bed, the attenuation is a function of the solids distribution: the more solids present on the beam, the higher the attenuation. Moreover, the walls of the fluidized bed will also contribute to the attenuation. This is incorporated in the measured number of photons per sample according to:

$$R = R_0 \exp\left[-\left((1-\alpha)\mu_\mathrm{p} + \alpha\mu_\mathrm{g}\right)d\right] \tag{2}$$

with R_0 the number of photons registered per second when the system is in vacuum; μ_p and μ_g denote the linear absorption coefficient of the particle and gas phase; α is the volume fraction of the gas phase; and d is the length of the inner path of the X-rays through the fluidized bed. This obviously depends on the particular X-ray beam that is measured. It should be noted that the attenuation characteristics of the fluidized bed wall are incorporated in R_0.

An X-ray source is not a monochromatic source: it generates a wide spectrum of X-ray energies. The attenuation coefficients, μ_p and μ_g, are functions of the photon energy E. For monochromatic photons, a two-point calibration is sufficient. This is easily achieved by performing a measurement with air only in the column and a second one under packed bed (or minimal fluidization) conditions. However, for X-ray sources with a wide energy spectrum, this is inadequate, as photons of lower energy are absorbed much faster. Thus, the more material there is on the X-ray beam, the higher the fraction of high energy photons will be. This is called beam hardening. An easy way out of this is performing a more elaborate calibration. The essence of the calibration is that it provides a one-to-one coupling between the measured photon count rate and the amount of powder on the X-ray beam. We have calibrated all detectors individually by placing various amounts of packed powder in between a source and its detectors. The amount of packed powder is put inside the column to ensure that the calibration encompasses the effects of the walls of the column. Furthermore, the calibration includes a completely empty and a completely filled bed. These two calibration points provide the upper and lower limit of the signal. We fitted a smooth function of the form $A_\mathrm{cal} + B_\mathrm{cal} \cdot \exp(-x/C_\mathrm{cal})$ to the data, with x the distance traveled by the beam through the powder phase. Although it has no direct physical meaning, this calibration curve can be seen as being described via an effective attenuation coefficient. Note that we do not rely on a physical interpretation of the fitted curve, other than that it establishes the one-to-one relation mentioned. Any smooth curve that is monotonically decaying as a function of the amount of powder on the X-ray beam is suitable. For every detector, an individual curve is obtained, see Ref. 21.

Tomographic reconstruction

The raw data comprise in our case of three times 30 detector signals per plane. Each detector signal is the time series of the attenuation of the corresponding X-ray beam over its straight path through the fluidized bed. From such a set, we need to reconstruct the solids distribution. For this purpose, we use an ART. Although significantly slower than, e.g., linear back projection, algebraic methods offer more flexibility in terms of limited data sets and are more appropriate for the CT configuration under consideration here. Detailed accounts of reconstruction techniques can be found in Refs. 22, 23, or 24.

The steps for a reconstruction are as follows. First, we use the calibration curve to convert the measured line-averaged attenuation into a line-averaged solids fraction. Second, we will reconstruct the solids fraction $\alpha(x,y)$ in a pixel representation of the cross section of the fluidized bed. Here, we use a square pixel array of 55 $\times$ 55 pixels. The cross section of the fluidized bed exactly fits in this square. All pixels outside the circle have a solids fraction of zero. Third, the reconstruction algorithm needs to find the particle distribution that fits best to the data.

For a given ray, traveling through the object, the total solids fraction on the line, p_i, referred to as ray sum, can be estimated as

$$\tilde{p}_i = \sum_{j=1}^{N} W_{ij}\alpha_j \tag{3}$$

with α_j the pixel-based value of the solids fraction distribution and W_{ij} the weighing factor for pixel j for the ith ray through the object. We use a linear weighing matrix W. Hence, the

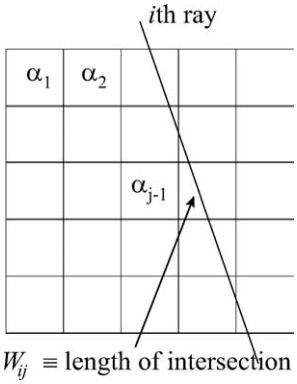

Figure 2. Definition of the elements of the W_{ij} matrix.

weighing factor W_{ij} is the length of ray i through pixel j, see Figure 2.

Fourth, to reconstruct the image we need to solve the unknown pixel-averaged solids fraction α_k from Eq. 3 for M different rays on N pixels. As the number of independent measurements is only 3*30 = 90 and the number of unknown pixels is easily 1000 or more, the problem is ill-posed. Moreover, there will be measuring noise in the data. The ART[22] are designed to minimize the mismatch between the data $\vec{p}$ and $\mathbf{W} \cdot \vec{\alpha}$. They are iterative methods that solve $\vec{p} = \mathbf{W} \cdot \vec{\alpha}$. We use the simultaneous algebraic reconstruction technique (SART).[25] Instead of sequentially updating the pixels on a ray-by-ray basis, SART simultaneously applies to a pixel the average of the corrections generated by all rays. This offers a reduction in the amplitude of the salt and pepper noise that is usually present in ART. However, it goes at the expense of the computation time.

The SART algorithm is given by:

$$\alpha_j^{n+1} = \alpha_j^n + \frac{1}{W_{+,j}} \frac{p_i - \tilde{p}_i}{W_{i,+}} W_{ij} \tag{4}$$

with $W_{+,j} = \sum_{i=1}^{M*M} W_{ij}$, $W_{i,+} = \sum_{j=1}^{N*N} W_{ij}$.

Pepper and salt noise in the images can be reduced by using a so-called one-step-late algorithm.[26] We invoked an algorithm based on the median root function (suggested first by Alenius and Ruotsalainen[27]). It effectively removes pepper and salt noise but keeps the edges of larger objects sharp enough. In the reconstruction algorithm, an extra step is added to Eq. 4:

$$\alpha_{\mathrm{OSL},j}^{n+1} = \frac{1}{1 + \beta \dfrac{\alpha_{\mathrm{OSL},j}^n - \mathrm{Med}(\alpha_{\mathrm{OSL},j}^n)}{\mathrm{Med}(\alpha_{\mathrm{OSL},j}^n)}} \alpha_j^{n+1} \tag{5}$$

with α_j^n the value of pixel j after the nth SART step and $\alpha_{\mathrm{OSL},j}^n$ the same after the nth one-step-late correction.

The median filter $\mathrm{Med}(\alpha_j)$ replaces the value of the j th pixel by the median of the pixel values contained in the j th pixel neighborhood. The definition of this pixel neighborhood is the only parameter of the median filter. We use a 3 $\times$ 3 neighborhood; a 5 $\times$ 5 neighborhood causes too much smearing. The parameter β in Eq. 5 controls the weight of the correction. We have set it to $\beta = 0.1$.

We use about 400 iterations per image. The lowest mismatch between the data and the prediction based on the reconstruction is usually found after about 1000 iterations. However, the difference between the image after 400 iterations and the best one is usually in a few pepper and salt pixels that are later, in the post processing step removed anyhow. A single image takes about 5–6 s on a 2 GHz CPU. The reconstruction program is coded in FORTRAN and runs on a stand-alone PC.

Experiments

The intensity of the generated photon beams fluctuates. This is an inherent aspects of X-ray sources. This noise corrupts the reconstructed images. Therefore, we have averaged the raw data first over 10 data points and moved in steps of 10 through the time series. Consequently, the time resolution of the images is 250 frames per second. For velocity measurements of bubbles that move from the lower measuring plane to the higher one, this would result in unwanted coarse discretization steps. A typical bubble velocity is some 50 cm/s. This means that there are about 10 images between the point in the image series where the bubble shows up in the lower plane and the corresponding passage in the upper plane. This gives a discretization step on the order of 4 cm/s. By using the raw signals directly, this can be reduced by an order of magnitude. Therefore, the velocity estimates are based on the raw data.

Velocity calibration

An air-filled cylinder of known size is pulled at constant velocity through the unfluidized bed. From the response of the detectors in the two planes, we can find the time it takes the cylinder to move from the lower plane to the upper one. As the cylinder velocity is measured independently, we can this way find the distance between the two planes.

To reduce the noise in the raw signals, we first denoised the raw data from the cylinder experiments using a Wavelet denoising. We used Daubechie wavelets for this purpose. Figure 3 shows the raw signal (dashed line) and the denoised one (solid line) for the passage of the cylinder as registered by the X-ray beam through the symmetry axis of the cylinder.

The cylinder is pulled upward via a copper rod that is attached to the top lid of the cylinder. The signal shown in Figure 3 comes from the X-ray beam that radiates straight through the rod. Therefore, the signal is at first relatively

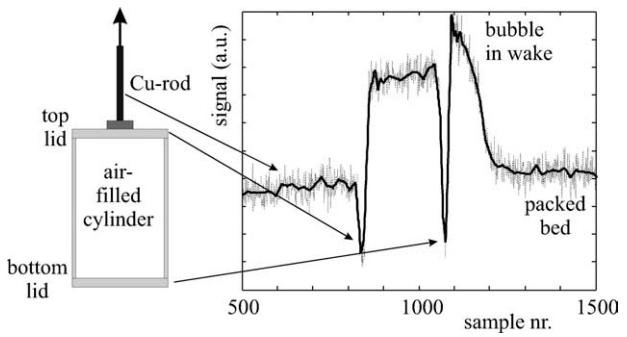

Figure 3. Raw signal (dashed, thin line) and denoised one (solid line).

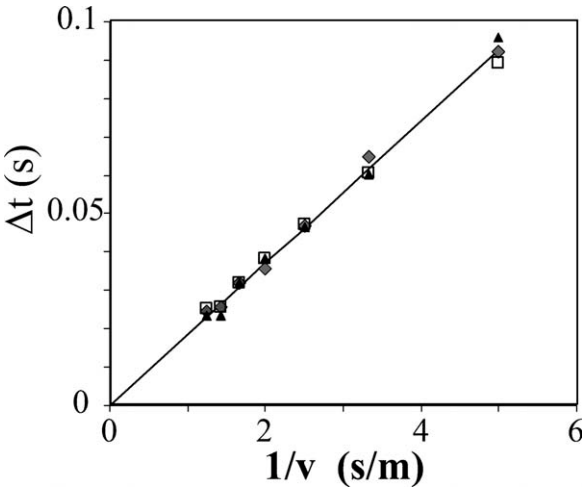

Figure 4. Average time of flight versus 1/*v* for all three X-ray beam pairs through the center of the cylinder.

Different symbols correspond to different beam-detector pairs.

low. The first peak downward is caused by the top lid of the cylinder that attenuates the signal even further. Next the signal increases as now the air-filled part of the cylinder moves over the X-ray beam. Subsequently, the bottom lid passes by, reducing the signal again. After this peak, the signal goes up again to an even higher value than the air-filled cylinder part. This is caused by an air bubble that is present in the wake of the upward moving cylinder. As this bubble has initially the same radius as the outer radius of the cylinder, but does not have a perspex wall, the attenuation is even further reduced and the signal is thus higher than that of the cylinder. Once this bubbles has passed the measuring plane, the level of the signal settles at the packed-bed level.

From either of the two peaks coming from the top and bottom of the cylinder as measured by the two corresponding detectors (one in the lower and one in the upper plane), the time of flight can be found. The averages for all three sources are given in Figure 4. As expected, the plot shows that the time of flight is a linear function of the inverse of the cylinder velocity. The best linear fit through the data is used as the calibration of the plane–plane distance. It is found to be 1.86 cm, which is close to the 2-cm distance based on geometrical arguments.

Bubble train

Next, the bed is set at minimal fluidization. A single capillary (inner diameter 4 mm) is inserted into the bed with its exit 132 mm above the porous plate of the fluid bed. Additional air flows through this capillary creating a train of bubbles. These bubbles rise upward and pass the two measuring planes, where they are detected. Data are taken for a period of 5 s. The raw data are grouped in sets of 10 samples, and the average of each set is calculated. From these, smoothed data reconstructions are computed. This generates 1250 images, separated by a time interval of 4 ms.

We performed a series of experiments with the fluidized bed positioned on a table that can be traversed in the vertical direction. We took measurements at different heights above the capillary exit, i.e., at 7, 17, 27, and 37 cm. We took two data sets (of 5 s each) per height. The gas flow rate through the capillary was set at 0.56 l/s. The velocity of the gas inside the capillary is 44 m/s. This means that we blow a jet of gas into the fluidized bed that breaks up in small bubbles.

The raw data are denoised using a Wavelet denoising. Next, from the time of flight of a bubble from the lower detector array to the upper one, the velocity of each bubble is obtained. The number of bubbles detected in the time interval of 5 s depends on the height above the capillary: we found 45 bubbles 7 cm above the capillary exit, 22 at a height of 17 cm, 13 at 27 cm, and 8 for the 37 cm case. The reconstructed images are stacked creating a 3D picture, see Figure 5 for an example at $h = 17$ and 37 cm, respectively. Note that the vertical axis is time with a scale in milliseconds.

The size of an individual bubble can be found by combining this time axis with the individual velocity of the bubbles. The bubble–bubble distance can only be estimated if we assume that the velocity of the bubbles is constant during the time interval between two subsequently passing bubbles. From the reconstructed bubbles, we have computed the bubble volume and from that the equivalent bubble diameter, $D_{eq} \equiv \left(\frac{6V_b}{\pi}\right)^{1/3}$. We expect that the bubbles at the lower heights above the capillary exit are smaller. Bubbles with a small separation distance might coalesce. Consequently, the number of bubbles passing a cross section of the fluidized bed per unit time will decrease. This is indeed what we observed. As mentioned, at the lower measuring plane we counted 45 bubbles in 5 s, and at the measuring plane at 17 cm above the capillary we found 22 bubbles also in a 5-s interval. This suggests that bubbles coalesce one time in

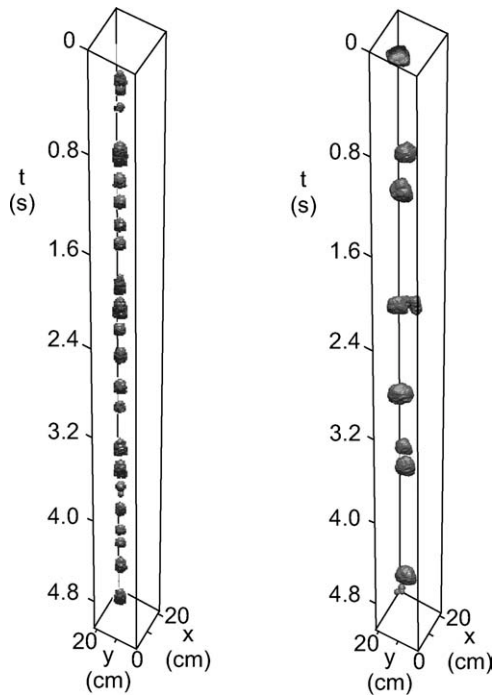

Figure 5. Reconstruction of the bubble train passing the measuring plane 17 cm (left) and 37 cm (right) above the capillary exit.

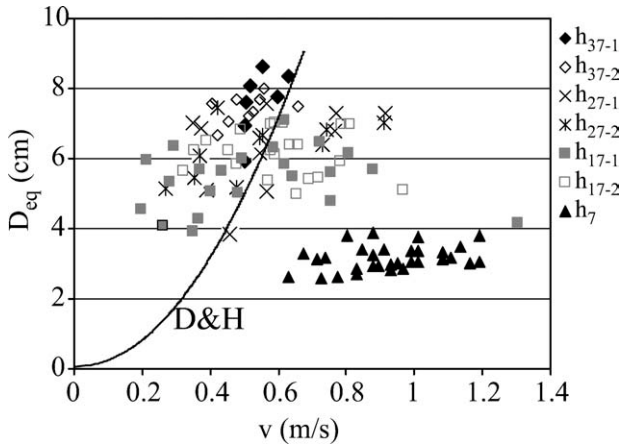

Figure 6. Equivalent diameter at four different heights. For every height two experiments are presented, except for h = 7 cm; ◇, for h = 37 cm, × for 27 cm, □, for 17 cm, and Δ for 7 cm above the capillary exit.

The solid line is the Davidson and Harrison correlation of a single rising bubble.

between these two planes. Assuming that the bubble volume is conserved during coalescence, this would mean that the ratio of the equivalent diameters at both heights should be 1.26.

As we see in the figure, the bubble equivalent diameter at 7 cm above the capillary is about 3 cm. At the next measuring plane this is 5.5 cm. From this, we conclude that the bubbles not only grow due to coalescence, as that would give a diameter of 4 cm. This suggests that the bubbles also suck in air from the fluidized powder. At 37 cm above the capillary exit the average equivalent diameter is about 7.6 cm. Here, we cannot draw firm conclusions, as the number of measured bubbles is at this height only 8 compared to 22 at the 17-cm level. Thus, on an average, bubbles have coalesced more than one but less than two times. Thus, according to coalescence, we should have sizes between 6.9 and 8.7 cm. We measured a size range from 7 to 9 cm. However, the set is too small for firm conclusions.

The rise velocity of the bubbles can be estimated from, e.g., the relation given by Ref. 28:

$$v_\infty = 0.711\sqrt{gD_b} \tag{6}$$

with v_∞ the terminal velocity of a single bubble in a fluidized bed at minimal fluidization, g the acceleration of gravity, and D_b the bubble diameter. Using the equivalent diameter this relation is also drawn in Figure 6. Clearly, the velocity of the bubbles close to the exit of the capillary is much higher than the Davidson and Harrison relation predicts. This is likely to be caused by the extra gas coming out of the capillary that does not end up in the bubbles, but moves through the powder phase. Hence, locally the interstitial gas velocity is much higher than that corresponding to minimum fluidization. Thus, the velocity predicted by the Davidson and Harrison relation should be extended. We use here to estimate the effect of the additional gas the Davidson and Harrison relation for the average velocity of a bubble in a freely bubbling bed:

$$v_b = (U - U_{mf}) + v_\infty \tag{7}$$

with U the actual superficial gas velocity. In the case of the jet, the additional gas will not be distributed immediately over the entire cross section of the bed. Instead, it will be localized around the bubble train. From the bubble frequency and the bubble size, we estimate the gas flow rate associated with the bubble phase: $Q_b = f_b V_b$. At a height of 7 cm above the capillary exit, we measured 45 bubbles in 5 s and found their diameter to be 3 cm. The gas flow rate through the capillary is $Q_{cap} = 0.56$ l/s. Thus, the additional gas flow rate through the powder phase is $Q_{cap} - Q_b = 0.43$ l/s. If we take for the area through which this additional gas is flowing a cylinder with a diameter on the order of the bubble size, the corresponding local superficial gas velocity is about 0.6 m/s. A bubble of 3 cm diameter has a rise velocity $v_\infty \approx 0.4$ m/s. Thus, we expect that the bubbles close to the capillary exit travel at a speed on the order of 1 m/s, which is indeed the magnitude seen in Figure 6. Higher above the capillary exit, the gas flowing in the form of bubbles is much closer to the additional gas flow rate through the capillary, e.g., at $h = 37$ cm we find $Q_{cap} - Q_b = 0.12$ l/s, which gives with the same reasoning an increase of the local superficial velocity on the order of only 1 cm/s. Consequently, the bubbles at this height move at the single bubble velocity.

The velocity of the bubbles is also influenced by the solids circulation induced by the rising bubble train. To estimate this effect, we assume that the particles in the wake of the bubbles are carried to the top of the bed and move downward in the annulus around the bubble train. The wake is estimated as half the bubble volume. The corresponding induced upward velocity of the powder phase is then $U_{sol,up} = \frac{Q_b}{2A_b} = \frac{1}{3} f_b D_{eq}$. Taking the values at a height of 37 cm, we compute an upward velocity of about 4 cm/s, which is much smaller than the bubble velocity itself.

Obviously, the computed equivalent diameter is depending on the velocity of a bubble. This might introduce a bias or large uncertainty. We can compare the equivalent bubble diameter with the bubble size based on the reconstructed images. These provide the size of the bubbles by measuring

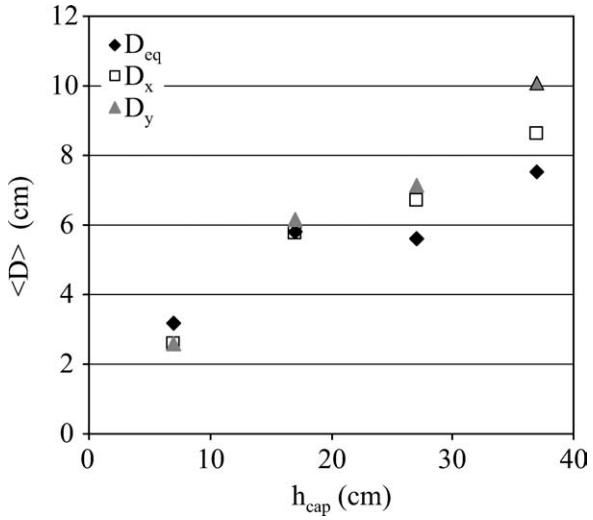

Figure 7. Equivalent diameter at four different heights.

the ''diameter'' in each reconstructed image. We use the two perpendicular axis of the grid. The x-axis is parallel to the central X-ray of the first source; the y-axis does not coincide with any of the X-rays. The average diameter in both directions for each of the measuring heights is computed. Together with the equivalent diameter, these averages are shown in Figure 7. From the figure, we see that the three estimates of the average bubble size are in reasonable agreement. The equivalent diameter and the other two do not have to coincide, as the bubbles are not really spherical. For the two other diameters, we expect a closer agreement. Especially at h = 37 cm, the difference between the diameter estimates is relatively large. At this point, more research is needed, with a larger set of bubbles to investigate whether there is a bias in the data analysis.

Concluding Remarks

This article deals with experiments in a 23-cm fluidized bed using a double X-ray tomographic scanner. We report a calibration procedure for finding velocities of bubbles passing two parallel measuring planes. We are able to find properties, such as size, volume, and velocity, of individual bubbles passing the measuring plane. The two measuring planes of the scanner are separated by 1.86 cm. Consequently, the time series we measured can be transformed to the vertical sizes of the bubbles. We performed experiments in which we release a train of small bubbles from a single capillary inserted into a minimal fluidized bed. We found that the bubbles grow while flowing upward. This growth is partially due to coalescence, but it seems also that close to the injection point the bubbles suck in additional air from the surrounding fluidized powder.

Our scanner is able to measure individual bubbles with an equivalent diameter of 2.5–3 cm and larger in a 23-cm-diameter fluidized bed. We reconstruct the solids distribution in a cross section of the fluidized bed at 250 frames per second. For the velocity of the individual bubbles, we used the time of flight of the passage from the lower to the upper measuring plane. The raw data are used to this end as these are sampled at 2500 Hz. To reduce the influence of noise, we first denoise the raw signals using the Daubechie wavelets. This gives a much better resolution for the velocity than working with the reconstructed images of the bubbles.

Literature Cited

1. Reinecke N, Mewes D. Recent developments and industrial research applications of capacitance tomography. *Meas Sci Technol*. 1996;7:233–246.
2. Kühn FT, Schouten JC, Mudde RF, Van den Bleek CM, Scarlett B. Analysis of chaos in fluidization using electrical capacitance tomography. *Meas Sci Technol*. 1996;7:361–368.
3. Beck MS, Dyakowski T, Williams RA. Process tomography—the state of the art. *Trans Inst Meas Control*. 1998;20:163–177.
4. Warsito W, Fan L-S. Neural network based multi-criterion optimization image reconstruction technique for imaging two- and three-phase flow systems using electrical capacitance tomography. *Meas Sci Technol*. 2001;12:2198–2210.
5. Warsito W, Fan L-S. Dynamics of spiral bubble plume motion in the entrance region of bubble columns and three-phase fluidized beds using 3D ECT. *Chem Eng Sci*. 2005;60:6073–6084.
6. Gladden LF, Anadon LD, Dunckley CP, Mantle MD, Sederman AJ. Insights into gas-liquid-solid reactors obtained by magnetic resonance imaging. *Chem Eng Sci*. 2007;62:6969–6977.
7. Dudukovic MP. Opaque multiphase reactors: experimentation, modeling and troubleshooting. *Oil Gas Sci Technol*. 2000;55:135–158.
8. Chaouki J, Larachi F, Dudukovic MP. Noninvasive tomographic and velocimetric monitoring of multiphase flows. *Ind Chem Eng Chem Res*. 1997;36:4476–4503.
9. Devanathan N, Moslemian D, Duduković MP. Flow mapping in bubble columns using CARPT. *Chem Eng Sci*. 1990;45:2285–2291.
10. Devanathan N, Duduković MP, Lapin A, Lübbert A. Chaotic flow in bubble columns. *Chem Eng Sci*. 1995;50:2661–2667.
11. Grevskott S, Sannæs BH, Duduković MP, Hjarbo KW, Svendsen HF. Liquid circulation, bubble size distributions, and solids movement in two- and three-phase bubble columns. *Chem Eng Sci*. 1996;51:1703–1714.
12. Guha D, Ramachandran PA, Dudukovic MP. Flow field of suspended solids in a stirred tank reactor by Lagrangian tracking. *Chem Eng Sci*. 2007;62:6143–6154.
13. Fangary YS, Barigou M, Seville JPK, Parker DJ. Fluid trajectories in a stirred vessel of non-Newtonian liquid using positron emission particle tracking. *Chem Eng Sci*. 2000;55:5969–5979.
14. Fishwick RP, Winterbottom JM, Parker DJ, Fan X, Stitt EH. Hydrodynamic measurements of up- and down-pumping pitched-blade turbines in gassed, agitated vessels, using Positron Emission Particle Tracking. *Ind Eng Chem Res*. 2005;44:6371–6380.
15. Kumar SB, Moslemian D, Duduković MP. Gas holdup measurements in bubble columns using computed tomography. *AIChE J*. 1997;43:1414–1425.
16. Kumar SB, Moslemian D, Duduković MP. A γ-ray tomographic scanner for imaging voidage distribution in two-phase flow systems. *Flow Meas Instrum*. 1995;6:61–73.
17. Shollenberger KA, Torczynski JR, Adkins DR, O'Hern TJ, Jackson NB. Gamma-densitometry tomography of gas holdup spatial distribution in industrial-scale bubble columns. *Chem Eng Sci*. 1997;52:2037–2048.
18. Mudde RF, Harteveld WK, Van den Akker HEA, Van der Hagen THJJ, Van Dam H. Gamma radiation densitometry for studying the dynamics of fluidized beds. *Chem Eng Sci*. 1999;54:2047–2054.
19. Bieberle M, Hampel U. Evaluation of a limited angle scanned electron beam x-ray CT approach for two-phase pipe flows. *Meas Sci Technol*. 2006;17:2057–2065.
20. Bieberle M, Fischer F, Schleicher E, Hampel U, Koch D, Aktay KSDC, Menz H-J, Mayer H-G. Ultrafast limited-angle-type x-ray tomography. *Appl Phys Lett*. 2007;91:123516.
21. Mudde RF, Alles J, Van der Hagen THJJ. Feasibility study of a time-resolving X-ray tomographic system. *Meas Sci Technol*. 2008;19:085501.
22. Brooks RA, DiChiro G. Principles of computer assisted tomography (CAT) in radiographic and radioscopic imaging. *Phys Med Biol*. 1976;21:689–732.
23. Herman GT. *Image Reconstruction from Projections—the Fundamentals of Computerized Tomography*. London: Academic Press, 1980.
24. Kak M, Slaney M. *Principles of Computerized Tomographic Imaging*. New York: IEEE Press, 1988.
25. Andersen AH, Kak AC. Simultaneous algebraic reconstruction technique (SART): a superior implementation of the ART algorithm. *Ultrason Imaging*. 1984;6:81–94.
26. Green PJ. Bayesian reconstruction from emission tomography data using a modified EM algorithm. *IEEE Trans Med. Imaging*. 1990;9:84–93.
27. Alenius S, Ruotsalainen U. Bayesian image reconstruction for emission tomography based on median root prior. *Eur J Nucl Med*. 1997;24:258–265.
28. Davidson JF, Harrison D. *Fluidized Particles*. Cambridge, UK: Cambridge University Press, 1963.

Manuscript received Jan. 21, 2010, and revision received Sept. 23, 2010.